A&A 537, A46 (2012)
DOI: 10.1051/0004-6361/201117883

Astronomy & Astrophysics

Magnetoacoustic waves in diagnostics of the flare current sheets

P. Jelínek[1] and M. Karlický[2]

[1] University of South Bohemia, Faculty of Science, Branišovská 10, 370 05 České Budějovice, Czech Republic
e-mail: pj@matfyz.cz
[2] Academy of Sciences of the Czech Republic, Astronomical Institute, v. v. i., Fričova 258, 251 65 Ondřejov, Czech Republic
e-mail: karlicky@asu.cas.cz

Received 15 August 2011 / Accepted 24 October 2011

ABSTRACT

Aims. To obtain diagnostics tools for solar flare current sheets, we numerically studied impulsively generated magnetoacoustic waves in the Harris current sheet.
Methods. We used two-dimensional (2-D) magnetohydrodynamic (MHD) and wave dispersion models. Tests of these models were performed for waves in the density slab, where analytical solutions are known. In the MHD model, we solved the full set of ideal MHD equations by means of the modified two-step Lax-Wendroff algorithm. The initial perturbation was chosen to generate preferentially the fast sausage magnetoacoustic waves. To determine the dispersion characteristics of MHD waves in the Harris current sheet, we numerically solved the equation of plasma motions by means of the Runge-Kutta fourth order method together with the bisection iteration one. To establish some diagnostics of these waves and their corresponding flare current sheets, we used the wavelet analysis method.
Results. We find that the results of tests of our 2-D MHD and wave dispersion models for the density slab are in good agreement with analytical results. We analyze the magnetoacoustic waves in the current sheet and compare them with those in the density slab. In both cases, for similar geometrical and plasma parameters, we find that wave trains were generated and propagated in a similar way. Their signals registered at selected locations of the Harris current sheet and density slab are also similar. Nevertheless, a dependence of the period of the magnetoacoustic waves on the width of the Harris current sheet differs from that for the density slab. The form of the wave front inside the current sheet similarly differs from that in the density slab. We find that the wavelet spectra of the signals of incoming magnetoacoustic waves at selected locations in the current sheet have the form of wavelet tadpoles. We distinguish that the form of these wavelet tadpoles becomes longer and the heads of the wavelet tadpoles are detected later in time as the distance of the detection point from that of the initial wave perturbation increases. We also find that the wavelet tadpole period depends on the plasma beta parameter. The results are discussed from the point of view of their use as diagnostics of the flare current sheets or flare loops.

Key words. methods: numerical – Sun: flares – Sun: oscillations – Sun: corona – magnetohydrodynamics (MHD)

1. Introduction

Oscillations and magnetohydrodynamic (MHD) plasma waves play a very important role in the many phenomena observed in the solar atmosphere (see e.g. Priest 1982; Aschwanden 2004). These MHD waves and oscillations have been analyzed by theoretical and numerical research Nakariakov et al. (2004, 2005), Selwa & Murawski (2004), Selwa et al. (2005, 2007), or Jelínek & Karlický (2009, 2010). The various oscillation modes in solar coronal loops have been observed with highly sensitive instruments such as SUMER (SoHO) and TRACE, as well as by more recent missions, e.g., EIS/Hinode or EUVI/STEREO. The observed oscillations include propagating waves similar to those of DeMoortel et al. 2002 and slow standing magnetoacoustic waves similar to those described by Ofman & Wang (2002), as well as a branch of fast magnetoacoustic waves, horizontal kink, vertical kink, and fast sausage waves (see e.g. Aschwanden 2004 or Wang & Solanki 2004).

The impulsively generated MHD waves and oscillations can be excited by various processes in the solar corona. The impulsive flare process, which provides either single or multiple sources of disturbances, is the most probable one. The impulsively generated magnetoacoustic waves are trapped in regions of higher density, i.e. in regions with a lower Alfvén speed, which act as waveguides. The periodicity of propagating fast sausage waves is formed by the time evolution of an impulsively generated signal (see Roberts et al. 1983, 1984; and Murawski & Roberts 1994). These waves in a coronal waveguide have three distinct phases: 1) periodic phase (long-period spectral components arrive as the first at observation point); 2) quasi-periodic phase (as both long and short-period spectral components arrive and interact), and finally; 3) decay (or Airy) phase (as the signal passes), (Roberts et al. 1984).

The wavelet analysis of impulsively generated (fast sausage) magnetoacoustic wave trains shows the typical tadpole shape where a narrow-spectrum tail precedes a broadband head. These tadpole signatures (wavelet tadpole) were firstly observed by the SECIS instrument in the 1999 solar-eclipse data (see Katsiyannis et al. 2003). Similarly, Mészárosová et al. (2009a,b) detected, for the first time, the tadpoles in the wavelet spectra in some radio sources, which have also been confirmed numerically, see e.g. Nakariakov et al. (2004, 2005).

Karlický et al. (2011) found the wavelet tadpoles in sources of narrowband dm-spikes. They concluded that these wavelet

tadpoles indicate that magnetoacoustic waves propagate in the global current sheet (current layer) in the turbulent reconnection outflows. This paper served as a motivation of a more extended and detailed study of magnetoacoustic (fast sausage) waves in the current sheet. In particular, much interest has been placed on the parameters of the current sheets (e.g. the current sheet width, the plasma beta parameter, and the distance between the wave initiation and detection sites) that influence the detected signal and its corresponding wavelet spectrum. Assuming that these waves modulate the radio fluxes (or even UV fluxes) in various locations of the current sheet, we propose that this knowledge can help us to determine the parameters of flare current sheets. For model tests and comparison, a similar study of the density slab was made. Therefore, a similar method can be used to determine the diagnostics of the density slabs, which correspond to flare loops in coronal conditions.

The structure of the present paper is as follows. Section 2 describes our numerical models, and Sect. 3 contains initial conditions and a form of initial perturbations. In Sect. 4, the numerical results, obtained by means of our computer models, are shown and discussed. Finally, in Sect. 5 our conclusions are presented.

2. Numerical model

2.1. Numerical solutions of MHD equations

In our present model, we describe the plasma dynamics by the ideal magnetohydrodynamic equations (see Priest 1982; Chung 2002)

$$\frac{\partial \varrho}{\partial t} = -\nabla(\varrho \boldsymbol{v}), \tag{1}$$

$$\varrho\frac{\partial \boldsymbol{v}}{\partial t} + \varrho(\boldsymbol{v}\nabla)\boldsymbol{v} = -\nabla p + \frac{1}{\mu_0}(\nabla \times \boldsymbol{B}) \times \boldsymbol{B}, \tag{2}$$

$$\frac{\partial \boldsymbol{B}}{\partial t} = \nabla \times (\boldsymbol{v} \times \boldsymbol{B}), \tag{3}$$

$$\frac{\partial U}{\partial t} = -\nabla \boldsymbol{S}, \tag{4}$$

$$\nabla \boldsymbol{B} = 0, \tag{5}$$

where ϱ is a mass density, $\boldsymbol{v}$ is the flow velocity, p is the gas pressure, and $\boldsymbol{B}$ is the magnetic field. The plasma energy density U is given by

$$U = \frac{p}{\gamma - 1} + \frac{\varrho}{2}v^2 + \frac{B^2}{2\mu_0}, \tag{6}$$

where the adiabatic coefficient is $\gamma = 5/3$, and the flux vector $\boldsymbol{S}$ is expressed as

$$\boldsymbol{S} = \left(U + p + \frac{B^2}{2\mu_0}\right)\boldsymbol{v} - (\boldsymbol{v}\boldsymbol{B})\frac{\boldsymbol{B}}{\mu_0}. \tag{7}$$

The magnetohydrodynamic Eqs. (1)–(4) were transformed into a flux conserving form, i.e.

$$\frac{\partial \boldsymbol{\Psi}}{\partial t} + \frac{\partial \boldsymbol{F}(\boldsymbol{\Psi})}{\partial x} + \frac{\partial \boldsymbol{G}(\boldsymbol{\Psi})}{\partial y} = 0, \tag{8}$$

and solved numerically. The vector $\boldsymbol{\Psi}$ in the two-dimensional case is expressed as

$$\boldsymbol{\Psi} = \begin{pmatrix} \rho \\ \rho v_x \\ \rho v_y \\ B_x \\ B_y \\ U \end{pmatrix}. \tag{9}$$

The vector functions $\boldsymbol{F}(\boldsymbol{\Psi})$ and $\boldsymbol{G}(\boldsymbol{\Psi})$ are too complex to be reproduced here, hence for more information we refer to either Sankaran et al. (2002) or Chung (2002).

For the numerical solution of this type of equations, we used the modified two-step Lax-Wendroff algorithm (Kliem et al. 2000). The numerical region was oriented in the x, y-plane, implemented at $0 \le x \le L$ and $0 \le y \le H$ and covered by a uniform grid with 1250×300 cells. Open boundary conditions were applied and the time step satisfied the Courant-Friedrichs-Levy condition in the form given by Chung (2002)

$$\Delta t \le \frac{\mathrm{CFL}\Delta x}{\max(c_\mathrm{s} + |\boldsymbol{v}|)}, \tag{10}$$

where CFL = 0.8 is called the Courant number.

To stabilize the-two step Lax-Wendroff numerical scheme, we applied artificial smoothing (see Sato & Hayashi 1979). At each grid point, all variables were replaced after each full time step of the algorithm according to the formula

$$\boldsymbol{\Psi}^n_{i,j} = \lambda\boldsymbol{\Psi}^n_{i,j} + \frac{1-\lambda}{4}(\boldsymbol{\Psi}^n_{i-1,j} + \boldsymbol{\Psi}^n_{i+1,j} + \boldsymbol{\Psi}^n_{i,j-1} + \boldsymbol{\Psi}^n_{i,j+1}), \tag{11}$$

with the coefficient $\lambda = 0.98$ during the simulation (see Kliem et al. 2000).

2.2. Calculations of phase and group speeds

For the calculations of phase and group velocities of plasma waves in current sheets and the density slab, we numerically solved the wave equation for plasma motions, as described by e.g. Smith et al. (1997), Roberts (1981a,b), or Edwin & Roberts (1982, 1983), where the equilibrium parameters of the loop (density and pressure) depend on the y coordinate

$$\frac{\mathrm{d}}{\mathrm{d}y}\left[f(y)\frac{\mathrm{d}v_y}{\mathrm{d}y}\right] + \varrho\left(\omega^2 - k_x v^2_\mathrm{Alf}\right)v_y = 0, \tag{12}$$

where v_y is the velocity component normal to the magnetic field, ω is the frequency, k_x is the longitudinal wavenumber along the sheet, and the Alfvén speed is calculated as $v^2_\mathrm{Alf} = B^2/\mu_0\varrho$.

The function $f(y)$ from Eq. (12) is expressed as

$$f(y) = \frac{\varrho c^2_\mathrm{f}\left(\omega^2 - k^2_x c^2_\mathrm{T}\right)}{\left(\omega^2 - k^2_x c^2_\mathrm{s}\right)}, \tag{13}$$

where $c_\mathrm{s} = (\gamma p/\varrho)^{1/2}$ is the sound speed. The tube speed c_T and fast speed c_f are implied as $c_\mathrm{T} = c_\mathrm{s}v_\mathrm{Alf}/(c^2_\mathrm{s} + v^2_\mathrm{Alf})^{1/2}$ and $c_\mathrm{f} = (c^2_\mathrm{s} + v^2_\mathrm{Alf})^{1/2}$, respectively.

Equation (12) has a singular point called either the cusp resonance or cusp singularity. This point plays an important role in the case of slow magnetoacoustic waves, whereas it is not seen in numerical simulations of the fast magnetoacoustic waves (see e.g. Zhukov 1989).

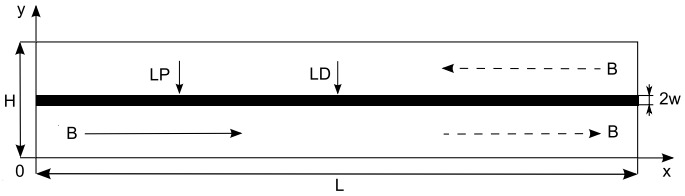

Fig. 1. The sketch of a 2-D Harris current sheet (or density slab) considered to be along the x-axis. Positions of the initial pulse L_P, data collection L_D, and magnetic field orientations are shown.

The second order ordinary differential Eq. (12) is rewritten in terms of two first order equations in the new functions ξ_1 and ξ_2

$$\xi_1 = f(y)\frac{\mathrm{d}v_y}{\mathrm{d}y}, \qquad \xi_2 = v_y, \tag{14}$$

such that

$$\frac{\mathrm{d}\xi_1}{\mathrm{d}y} = \varrho\left(k_x v_{\mathrm{Alf}}^2 - \omega^2\right)\xi_2, \tag{15}$$

and

$$\frac{\mathrm{d}\xi_2}{\mathrm{d}y} = \frac{\xi_1}{f(y)}. \tag{16}$$

The boundary conditions at the point $y = 0$ for the "kink" mode are given by $\xi_1 = 0, \xi_2 = c$. The "sausage" mode satisfies the conditions $\xi_1 = c\,f(0), \xi_2 = 0$, whereas the constant c is arbitrary in both cases.

To obtain a solution of Eq. (12) we used a fixed value of k_x and integrating between $y = 0$ and $y = y_{\max}$ the two first order Eqs. (15) and (16) by means of the Runge-Kutta fourth order method. The exact value of the frequency ω was obtained with the bisection iteration method when the velocity v_y satisfied the boundary condition at the second point $v_y(y = y_{\max}) = 0$ for both wave modes (kink and sausage mode).

3. Initial conditions and perturbations

The sketch of the studied two-dimensional (2-D) solar coronal structure is shown in Fig. 1. The arrows show the positions of the initial perturbation at L_P, the point where the data were detected at L_D, and the orientation of the magnetic field in both of the studied cases, the first the density slab with the parallel magnetic field (solid arrow) and the second the Harris current sheet (dashed arrows).

The length and width of the simulation region, for both studied cases, were $L = 100$ Mm and $H = 24$ Mm, respectively.

In the dense part of the density slab and the whole simulation box of the Harris current sheet, the temperature was assumed to be constant, at $T = 10^7$ K, and the corresponding sound speed is $c_s \approx 166\,T^{1/2} = 525$ km s^{-1} (see Priest 1982). In the state of equilibrium, we assumed the initial plasma velocity $\boldsymbol{v} = 0$ and calculated the initial energy density U_0 from Eq. (6).

In view of our interest in studying impulsively generated wave trains in the solar coronal structures, we launched a pulse in the velocity in the y-axis direction. The point where the velocity is perturbed was located at $(L_P, H/2)$, (see Fig. 1) and the initial velocity pulse followed a (Gaussian) profile (see e.g. Nakariakov et al. 2004, 2005)

$$v_y = A_0\frac{y}{\lambda_x}\exp\left[-\frac{(x - L_P)}{\lambda_x}\right]^2\exp\left[-\frac{(y - H/2)}{\lambda_y}\right]^2, \tag{17}$$

where $A_0 = 1.5 \times 10^4$ m s^{-1} is the initial amplitude of the pulse, and $\lambda_x = 1.5$ Mm and $\lambda_y = 0.5$ Mm are the widths of the velocity pulse in the longitudinal and transverse directions, respectively. This type of pulse generates preferentially the sausage waves. The initial pulse in the velocity was generated at the start of the numerical simulation at time $t = 0$ s.

3.1. Density slab

The flare loop in this case is represented by a slab with a half-width $w = 1$ Mm. The slab is embedded in a magnetic environment with a magnetic field given by the plasma beta parameter

$$\beta = \frac{p}{p_{\mathrm{mag}}} = \frac{2\mu_0 p}{B^2}, \tag{18}$$

where the plasma beta β is assumed to be 0.1. The magnetic field is parallel to the x-axis (see Fig. 1) and is assumed to be constant in the whole simulation region.

The mass density profile in a flare loop along the x-axis is also considered to be constant, and along the y-axis the mass density profile is expressed by the formula (see Nakariakov & Roberts 1995)

$$\varrho(x, y) = \varrho_0 + (\varrho_{\mathrm{sl}} - \varrho_0)\,\mathrm{sech}^2\left\{\left[\frac{(y - H/2)}{w}\right]^{\alpha}\right\}, \tag{19}$$

where the power index α determines the steepness of the profile. The cases where the power index α equals either unity or infinity correspond to the symmetric Epstein profile or to the step function profile, respectively (see Nakariakov et al. 2005). In this study, $\alpha = 8$ was used for the calculations. The exact values of the mass density of the magnetic environment ϱ_0, as well as the mass density in the center of the slab ϱ_{sl} is given in Sect. 4.

3.2. Harris current sheet

The magnetic field in this current sheet is given by the equation

$$\boldsymbol{B} = B_{\mathrm{out}}\tanh\left[\frac{(y - H/2)}{w_{\mathrm{cs}}}\right]\hat{\boldsymbol{e}}_x, \tag{20}$$

where B_{out} is the magnetic field at $y \to \infty$ and w_{cs} is the half-width of the current sheet, $w_{\mathrm{cs}} = 1$ Mm.

Magnetic field B_{out} is determined from the equation

$$B_{\mathrm{out}} = \sqrt{\frac{2\mu_0 p_{\mathrm{cs}}}{1 + \beta}}. \tag{21}$$

The kinetic pressure at the center of the current sheet p_{cs} is calculated from the plasma density at the center of the current sheet ϱ_{cs}. We assumed that the plasma beta parameter outside of the current sheet is the same as in the case of density slab, i.e. $\beta = 0.1$.

Because of the zero magnetic field at the center of the current sheet $B_{\mathrm{cs}} = 0$, one can calculate, from the condition of equilibrium, of

$$p + \frac{B^2}{2\mu_0} = \mathrm{const.}, \tag{22}$$

that the distribution of the mass density in the simulation box is as follows

$$\varrho(x, y) = \varrho_{\mathrm{cs}} - \frac{mB_x^2(y)}{2\mu_0 k_{\mathrm{B}} T}, \tag{23}$$

where m is the proton mass, μ_0 is the magnetic permeability, and k_{B} is the Boltzmann constant.

4. Results

We present our numerically obtained results, firstly for the simple density slab and the Harris current sheet and secondly by comparing the numerical results for both magnetic structures.

4.1. Density slab

We show the results that we obtained for a simple flare loop – density slab in the magnetic field oriented parallel to the slab. We analyzed the incoming signal and compared the calculated period of the wave signal by the wavelet method with the analytical formula. The location of the perturbation point was $L_P = \{L/6, H/2\}$ and the position of the point where the data were collected was $L_D = \{L/2, H/2\}$, respectively (see Fig. 1).

To estimate the period of the wave signal, we use the equation provided by Roberts (1984)

$$P = \frac{2\pi w}{j_0 v_{Alf}} \sqrt{1 - \frac{\varrho_0}{\varrho_{sl}}} \approx 2.6 w / v_{Alf}, \quad (24)$$

where ϱ_0 and v_{Alf} are the values of mass density outside and the Alfvén speed inside the density slab, respectively. The square root in the Eq. (24) can be neglected when $\varrho_{sl} \gg \varrho_0$; we then obtain the period in the form shown on the right side of the equation, because $j_0 \approx 2.4$ is the first zero of the Bessel function $J_0(x)$.

In the presented case, the mass density of the magnetic environment is $\varrho_0 = 6.082 \times 10^{-12}$ kg m^{-3} and the mass density at the center of the slab is $\varrho_{sl} = 6.688 \times 10^{-11}$ kg m^{-3}, i.e. the mass density ratio $d = \varrho_0/\varrho_{sl} \doteq 0.091$. Thus, from Eq. (24) we obtained the period of the wave signal $P \approx 6.8$ s.

In Fig. 2, we also compare the results of different numerical tests. In its upper part, the time evolution of the incoming signal and the times when the first signal is detected T_{fs}, as well as the time of the decay phase T_{dp}, is shown. In the middle panel, the global wavelet spectrum of the incoming signal (full line) with the dominant wave period P, and the 99% significance level (dash-dotted line) (see Torrence & Compo 1998) is shown. The most dominant period in this wavelet spectrum is the period $P \approx 7.0$ s. This "mean" period is in good agreement with that given by the analytical Eq. (24), derived for the typical period of oscillation in the density slab. Finally, in the bottom part of the figure, we display the group speed of the wave v_{gr}.

To asses the quality of our numerical model, we calculated the wave periods for different half-widths of the density slab (see Table 1 second column). The computed values show a linear dependence on the density slab half-width w, which is in agreement with the analytical Eq. (24).

To estimate the time of the decay (Airy) phase of the wave signal, we found the minimum of the group velocity, (see Fig. 2 bottom), $v_{gr}^{min} = 0.2542 v_{Alf,0} = 3.27 \times 10^5$ m s^{-1}, where $v_{Alf,0}$ is the Alfvén speed outside the density slab. The time of decay phase is then $T_{dp} = |L_D - L_P|/v_{gr}^{min} \approx 102.0$ s (see Roberts et al. 1984). The time, when the first signal arrived is calculated as $T_{fs} = |L_D - L_P|/v_{Alf,0} = 25.9$ s, which should be compared with these values in the upper panel of Fig. 2.

Our presented results served mainly to verify that our numerical code works properly and the numerical results are comparable to the results obtained by means of known analytical formulae. After these successful tests, we applied our numerical codes for the calculations to more complicated structures in the solar corona, such as the Harris current sheet.

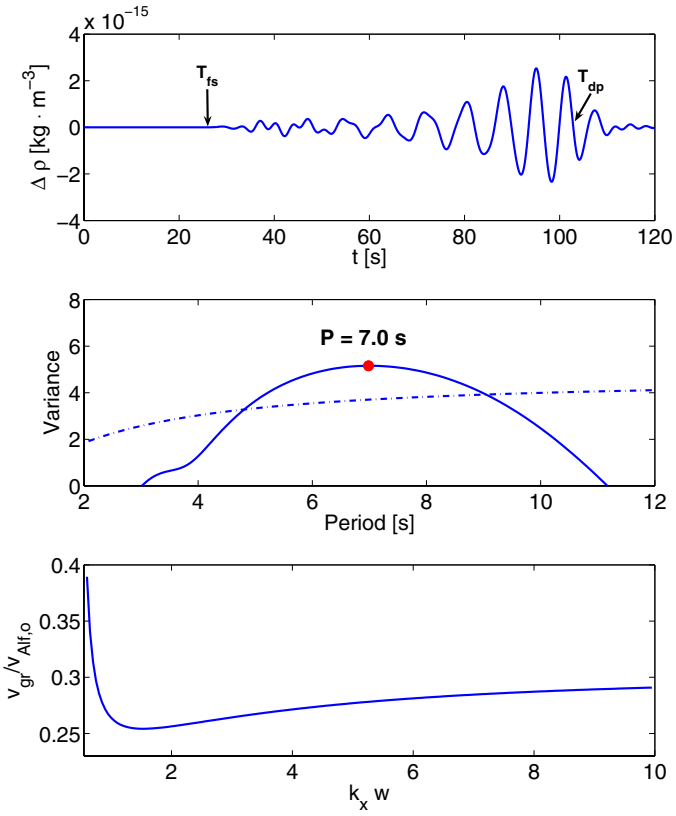

Fig. 2. *Upper panel*: time evolution of the mass density $\varrho(L_D = \{L/2, H/2\}, t)$. *Middle panel*: the global wavelet spectrum of the incoming signal (full line) with dominant wave period P, and the 99% significance level (dash-dotted line). *Bottom panel*: the group speed of the wave $v_{gr} = d\omega/dk$ in units of the external Alfvén speed as a function of wave number $k_x w$ (bottom panel). All for the density slab.

Table 1. Wave periods calculated by wavelet analysis for three selected half-widths w.

w [Mm]	P_{slab} [s]	P_{CS} [s]
1.00	7.0	6.8
1.25	8.6	7.6
1.50	10.4	8.2

Notes. Periods for the density slab (second column) and for the Harris current sheet (third column) are shown.

4.2. Harris current sheet

We present the numerical results obtained for the Harris current sheet configuration. We compare our results for different widths of the current sheet as well as for different plasma beta parameters.

In this studied case, we used values of the mass density similar to those of simple density slab, i.e. the mass density outside the Harris current sheet was $\varrho_0 = 6.082 \times 10^{-12}$ kg m^{-3} and the mass density at the center of the current sheet was $\varrho_{CS} = 6.688 \times 10^{-11}$ kg m^{-3}. The location of the point where the velocity is perturbed was placed at $L_P = \{L/6, H/2\}$ and the position of the detection point was assumed to be $L_D = \{L/2, H/2\}$, respectively.

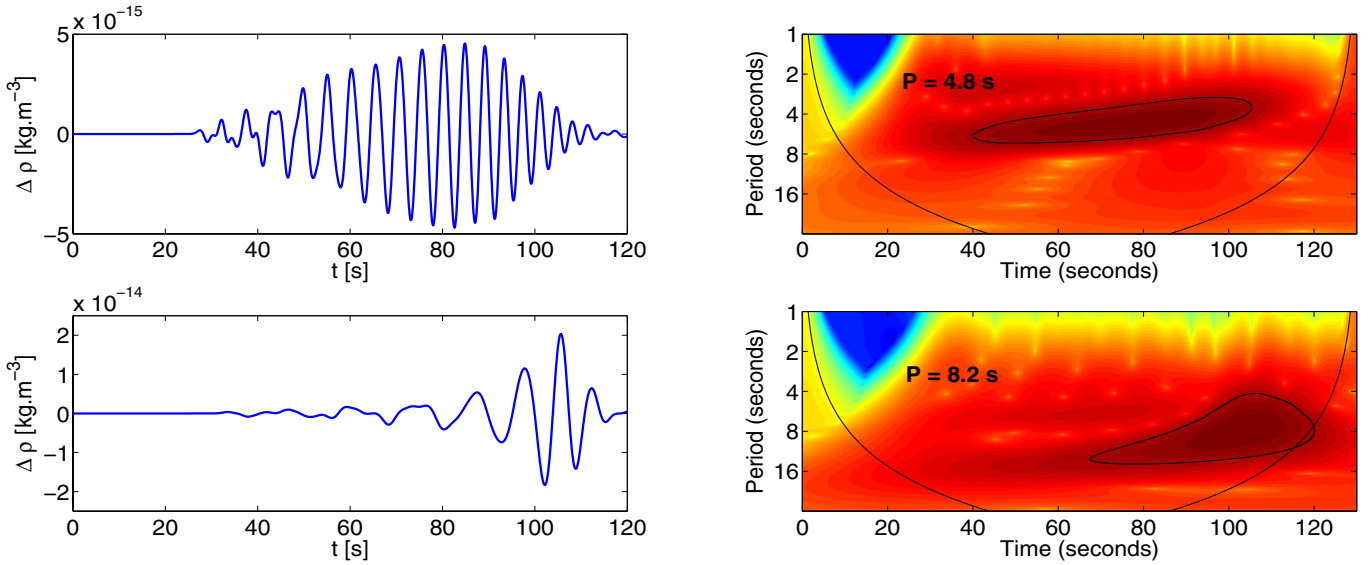

Fig. 3. Comparison of wave signals (*left column*) and corresponding wavelet tadpole shapes (*right column*) for two different widths of the Harris current sheet; $w_{CS} = 0.50$ Mm (*first row*) and $w_{CS} = 1.50$ Mm (*second row*). The data were recorded in the position $L_D = \{L/2; H/2\}$.

4.2.1. Current sheet width

In Fig. 3, we compare the of wave signals and the corresponding wavelet tadpole shapes for two different widths of the Harris current sheet. For the calculations, we used the widths of the Harris current sheet $w_{CS} = 0.50$ Mm and $w_{CS} = 1.50$ Mm. The plasma beta parameter was $\beta = 0.1$.

The figure shows that as the width of the Harris current sheet increases, the wave period also increases. However, this increase in the wave period is smaller than that for the density slab, as can be seen comparing the second and third columns of Table 1. Analyzing this difference, we conclude that it is caused by differences in the density and magnetic field profiles of both structures. In the density slab, its boundaries are similar to those of a step function for a broad range of half-widths (as in the analytical approach), while the current sheet profile becomes broader and less steep as the half-width increases. We also analyzed the average propagation speeds in the density slab and current sheet and found that after increasing the widths of both structures their average propagation speeds insides them remain practically the same. The average propagation speeds in the density slab and the current sheet for the same width are comparable. Considering these results and the values of the periods shown in Table 1, we can conclude for the current sheet that, if there is a relation similar to that for the density slab (Eq. (24)), then the constant of the proportionality in this relation for the current sheet is a slowly decreasing function with the increasing width of the current sheet, instead of the constant 2.6 for the density slab (Eq. (24)).

The wavelet analysis of the wave signal also reveals that for higher values of the Harris current sheet half-width, the wavelet tadpoles become shorter and the heads of the wavelet tadpoles are more distinct. These results agree with those presented in Nakariakov et al. (2005), where the longitudinal driver width was varied for a fixed width of the density slab. As shown by Nakariakov et al. (2005), narrower longitudinal drivers produce a broader k-spectrum above the cutoff for wave propagation and thus a broader interval of periods is detected.

4.2.2. Plasma beta parameter

Figure 4 shows the comparison of wave signals and corresponding wavelet tadpole shapes for two different plasma beta parameters. We present the results for plasma beta parameter $\beta = 0.01$ and $\beta = 0.05$, which are typical of values in the solar corona (see Aschwanden 2004).

We found that the higher the plasma beta parameter is, the shorter is the observed wave period. We compare these results with the value of the wave period in Fig. 11 (right column) for a plasma beta parameter $\beta = 0.1$.

We can also see that the changes in the plasma beta parameter have almost no effect at all on the shapes of the wavelet tadpoles. However, the time of the "first" signal is later in the case of a lower value of the plasma beta parameter. This is because when the plasma beta parameter decreases, the external Alfvén speed $v_{Alf,0}$ increases, hence the arrival time of the first signal decreases.

In Fig. 5, we depict the group speeds of the magnetoacoustic waves for two different plasma beta parameters. The graphs show the positions and values of the minimum group speeds $v_{gr,min}$.

The minima of the group speed for the plasma beta parameter of $\beta = 0.05$ were found to be $v_{gr,min} = 0.18 v_{Alf,0} = 3.27 \times 10^5$ m s^{-1}, and for a plasma beta $\beta = 0.10$ the minimal value of the group speed was $v_{gr,min} = 0.26 v_{Alf,0} = 3.34 \times 10^5$ m s^{-1}, respectively. In spite of the different ratio of minimal group speed to external Alfvén speed $v_{gr,min}/v_{Alf,0}$ for both of the studied cases, the time of the decay (Airy) phase is very similar (because of the very similar minimal group speeds $v_{gr,min}$) at $T_{dp} \approx 110$ s (see Fig. 4 for comparison).

4.3. Comparison of the density slab and the Harris current sheet

To compare the numerical results obtained for the density slab and the Harris current sheet, we use the physical quantities $\beta = 0.1$, $w_{sl} = w_{CS} = 1.0$ Mm.

The perturbation point was located at $L_P = \{L/6, H/2\}$ for all cases that we studied and compared, whereas the detection

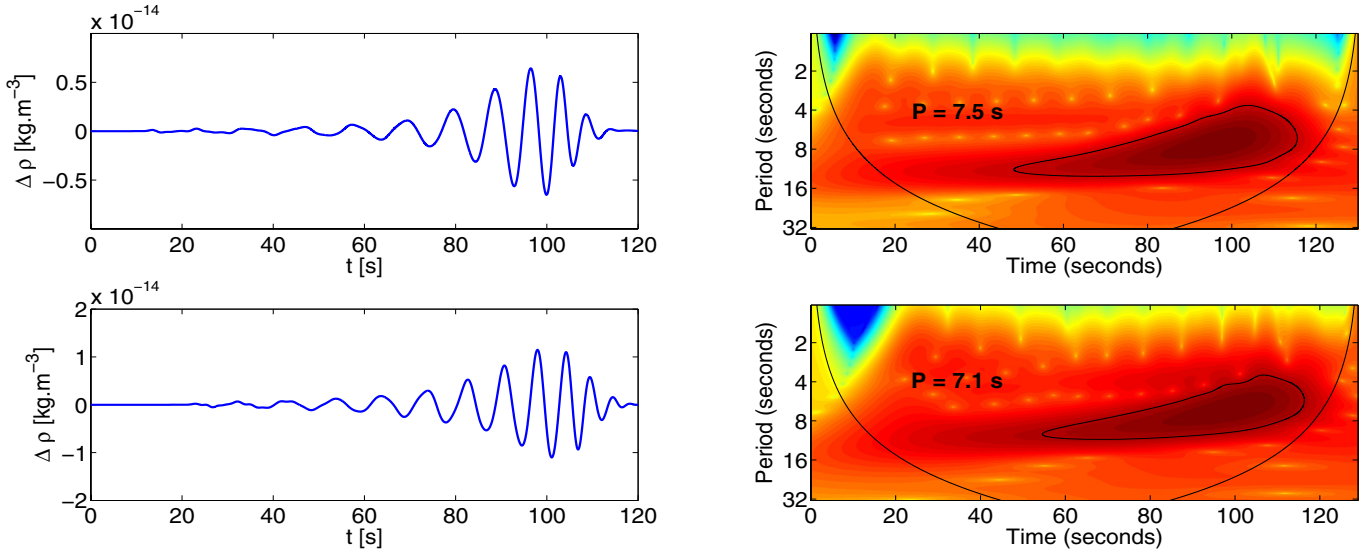

Fig. 4. Comparison of wave signals (*left column*) and corresponding wavelet tadpole shapes (*right column*) for plasma beta parameters $\beta = 0.01$ (*first row*) and $\beta = 0.05$ (*second row*), calculated for the Harris current sheet. The data were recorded in the position $L_D = \{L/2; H/2\}$.

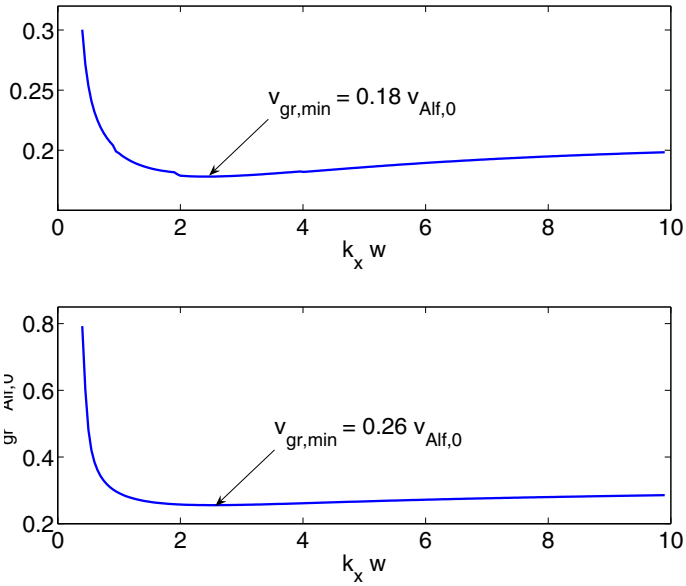

Fig. 5. Group speeds of the waves in units of the external Alfvén speed $v_{Alf,0}$ as the functions of wave number $k_x w$ for plasma beta parameter $\beta = 0.05$ (*upper panel*) and $\beta = 0.10$ (*lower panel*). The minimal values of the group speed v_{gr} are shown by arrows, and calculated for the Harris current sheet.

point L_D was placed at several points in the x-y plane to help improve our understanding of the nature of incoming wave signals.

4.3.1. Wave propagation

The numerical results calculated for the density slab (Fig. 6) and the Harris current sheet (Fig. 7) are compared. In both of these figures, we present the pressure variance $\Delta p = p(t) - p(0)$ at various times t during the wave evolution.

Comparing the contours of the pressure variance Δp, we can see that from the global point of view the results are similar. Nevertheless, when we study our resuts in detail (see e.g. Figs. 8 and 9), we can recognize differences, especially in the central parts of both the structures, where, in the Harris current sheet, the magnetic field, as well as the Alfvén speed is close to zero.

Since the wave evolution in the waveguide is determined by the dispersive properties of the waveguide as a whole, the global similarity of the evolution of both of these structures means that these structures have similar dispersive properties. However, differences found between the central parts of these structures are caused by local differences between the magnetic field and density profiles.

4.3.2. Incoming signals at different detection points

We compare the various wave signals entering the Harris current sheet in Fig. 10. To display the incoming wave signal, we used the time evolution of the mass density variance $\Delta\varrho = \varrho(t) - \varrho(t)$ at the detection point L_D. The point L_D where the data were collected was placed at six different positions in the numerical box. The three rows correspond to three points in the x-direction ($L/4$, $L/2$, and $3L/4$), whereas the two columns of the figure correspond to two points in y-direction ($H/2$ and $3H/4$).

When we compare the two columns of Fig. 10, it is evident that the signal at the center of the Harris current sheet has the shape, consisting of distinct phases, described in Roberts (1984). Using the wavelet analysis method, the typical tadpole shape was obtained (see Fig. 11). It is also clearly visible that the number of wavelengths depends on the position of the detection point L_D. This is again because the first waves to arrive are the fastest ones. The farther away the detection point is, the more waves (long and short period waves) are mixed.

On the other hand, from the second column of both figures we can see that the changes in the density variance here are not as high as at the center of the Harris current sheet. The shapes of these signals also differ from those in the first column. These signals are probably a mixture of several waves.

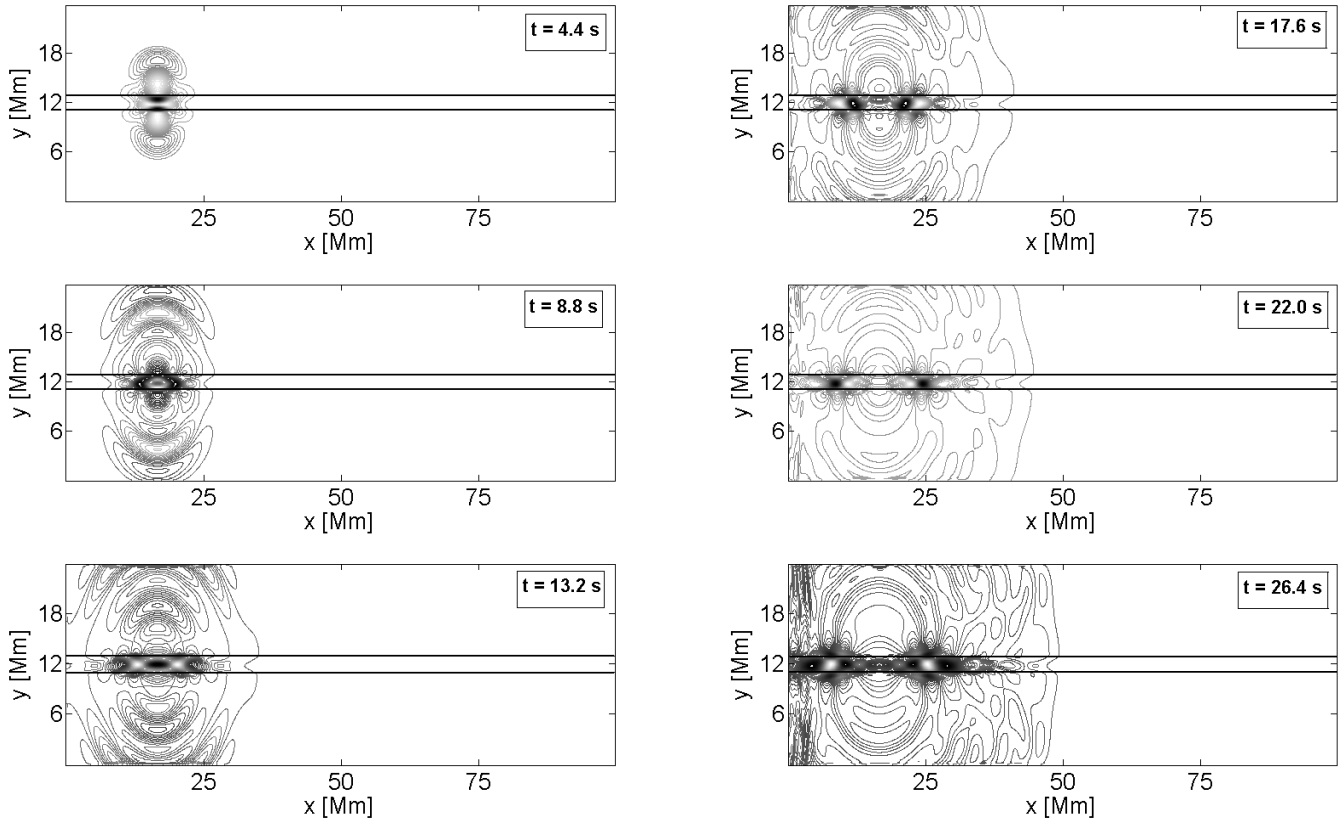

Fig. 6. The time evolution of the pressure variance $\Delta p = p(t) - p(0)$ at various times t, depicted as the contours for the density slab. The borders of the density slab are drawn as the black lines (w_{sl} = 1.0 Mm).

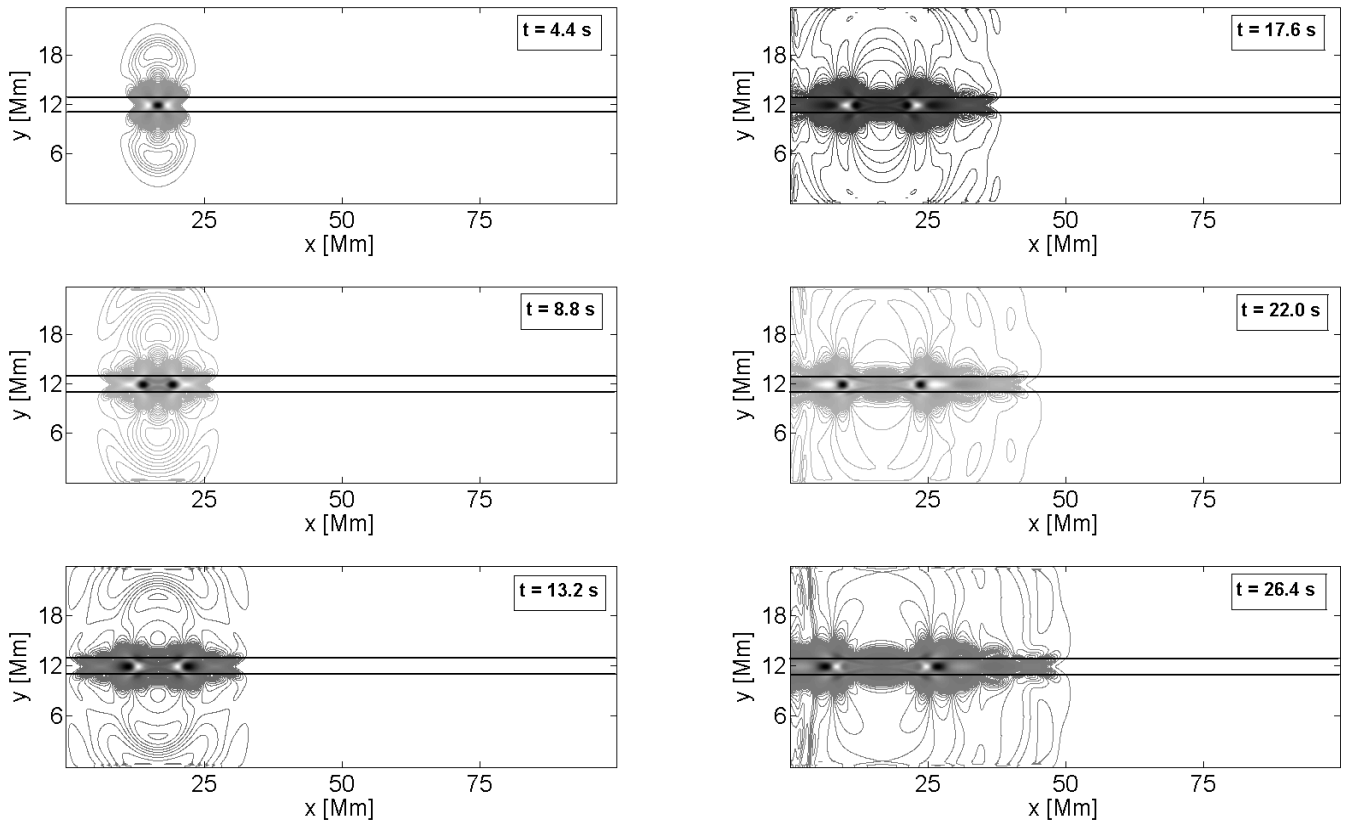

Fig. 7. The time evolution of the pressure variance $\Delta p = p(t) - p(0)$ at various times t, depicted as the contours for the Harris current sheet. The width of the current sheet is bordered by black lines (w_{CS} = 1.0 Mm).

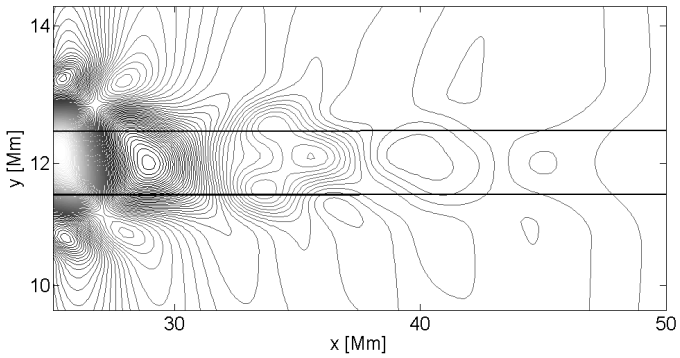

Fig. 8. Detail of the pressure variance Δp at the time $t = 26.4$ s for the density slab. The black lines represent the borders of the density slab ($w_{\rm sl} = 1.0$ Mm).

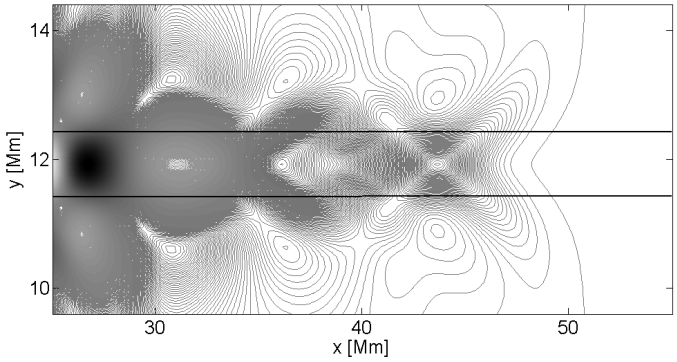

Fig. 9. Detail of the pressure variance Δp for the Harris current sheet at the time $t = 26.4$ s. The black lines represent the borders of the current sheet ($w_{\rm CS} = 1.0$ Mm).

4.3.3. Forms of wavelet tadpoles

Figure 11 shows the wavelet tadpoles calculated by means of the wavelet analysis for three different positions of the detection point, $L_{\rm D} = \{L/4, H/2\}, \{L/2, H/2\}$, and $\{3L/4, H/2\}$, in the density slab and in the Harris current sheet – as shown in the left and right column, respectively.

The shapes of the wavelet tadpoles of both of these structures were found to be very similar at all detection points. This is in good agreement with our previous findings about the behavior of the magnetoacoustic waves close to the center of the Harris current sheet. The form of these wavelet tadpoles becomes longer and the heads and tails of the wavelet tadpoles are detected later in time as the distance $|L_{\rm D} - L_{\rm P}|$ of the detection point increases away from that of the initial wave perturbation. The evolution of the detected signal with time is in good agreement with our expectations based on the analytical expressions for the estimation of the "first signal" arrival as well as the time of the decay (Airy) phase. The prolongations of the wavelet tadpoles, which depend on the location of the detection point $L_{\rm D}$, are due to the mixing of different phases of incoming magnetoacoustic waves and are in ratios of detection and perturbation point distances.

In the same figure, it can be seen that the periods of these wavelet tadpoles partly change because of the way in which they depend on the position of the detection point $L_{\rm D}$. From the global wavelet spectrum, we have found that the periods of the wave signals for the density slab and the Harris current sheet are as follows: $P_{L/4} = 6.8$ s, $P_{L/2} = 7.0$ s, $P_{3L/4} = 7.3$ s and, $P_{L/4} = 6.3$ s, $P_{L/2} = 6.8$ s, $P_{3L/4} = 7.2$ s, respectively.

5. Conclusions

Using the 2-D MHD model, we have studied numerically the propagation of magnetoacoustic waves in two different structures: a) the density slab with the straight magnetic field oriented along this slab; and b) the Harris current sheet. To obtain the phase and group speeds of propagating magnetoacoustic waves, we have numerically solved the wave equation of plasma motions. For the analysis of numerically calculated wave signals, we used the wavelet method.

In the case of the density slab, we compared the results of our numerical computations with analytical expressions. We found that the numerically obtained periods of wave signals, as well as their dependence on the slab half-width, are in good agreement with those calculated using analytical formulae. We compared how the times of the wave signal arrivals depend on the position of the detection point $L_{\rm D}$ using the numerically calculated and analytically derived group speeds of this wave. Since there was good agreement between the numerical and analytical results, we applied the numerical model for the Harris current sheet. The mutual comparisons of the results were made for both of these studied cases.

We found that from a global point of view magnetoacoustic waves in both cases evolve in a similar way. Nevertheless, there are differences in the central parts of these structures because of their different magnetic field profiles. Owing to the same reason, the dependences of the wave period on the half-width of these structures partly differ.

Considering these similarities and differences, one can conclude that without any additional information (e.g. information about the radio source location) it will not be easy to distinguish, in terms of diagnostics, between both of these cases. There may be an opportunity to resolve them in the form of the wavelet spectra derived e.g., in the analysis of the flare radio emission during solar flares (Mészárosová et al. 2009c). In particular, some unusual wavelet tadpoles have already been simulated, as well as observed, that be able to resolve these cases. However, this is beyond the scope of this paper and will be studied in more detail in further studies.

From the point of view of the diagnostics of either flare current sheets or flare loops, the most important measurements and findings are: a) the periods that can be used to estimate the half-width of these structures; and b) that the wavelet tadpoles become longer and their heads are detected later in time when increasing a distance between the detection and perturbation points. Thus, it is possible to estimate a distance between the radio source, for which modulated signal is analyzed, and the region where the magnetoacoustic wave is initiated. In special cases, we can even record the magnetoacoustic wave propagating along the density slab or the current sheet. For example, we can permit the magnetoacoustic wave to propagate along these structures upwards in the solar atmosphere and ensure that this wave modulates the radio emission (produced by the plasma emission mechanism) at lower radio frequencies. The wavelet spectra at these frequencies would then show us how the wavelet tadpoles have shifted in time, corresponding to the propagating magnetoacoustic wave train. Each tadpole corresponds to a specific plasma frequency, i.e. to specific plasma density and height in the solar atmosphere, if some density model of the solar atmosphere is assumed.

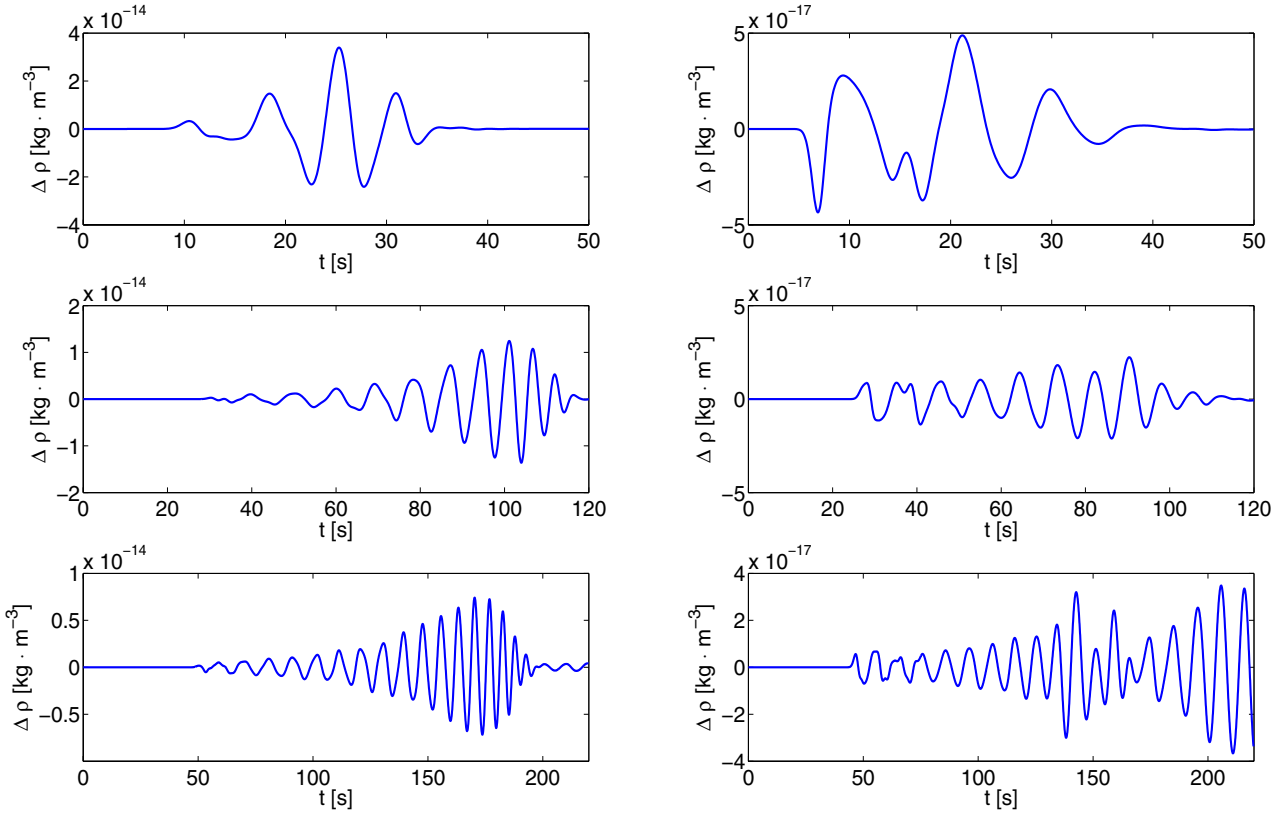

Fig. 10. Comparison of incoming wave signals in selected detection points. The data were recorded in $L_D = L/4, L/2, 3L/4$ (*upper, middle and lower panel*, respectively). In the *left and right columns*, the results for the center ($H/2$) and 75 Mm ($3H/4$) above the Harris current sheet are shown.

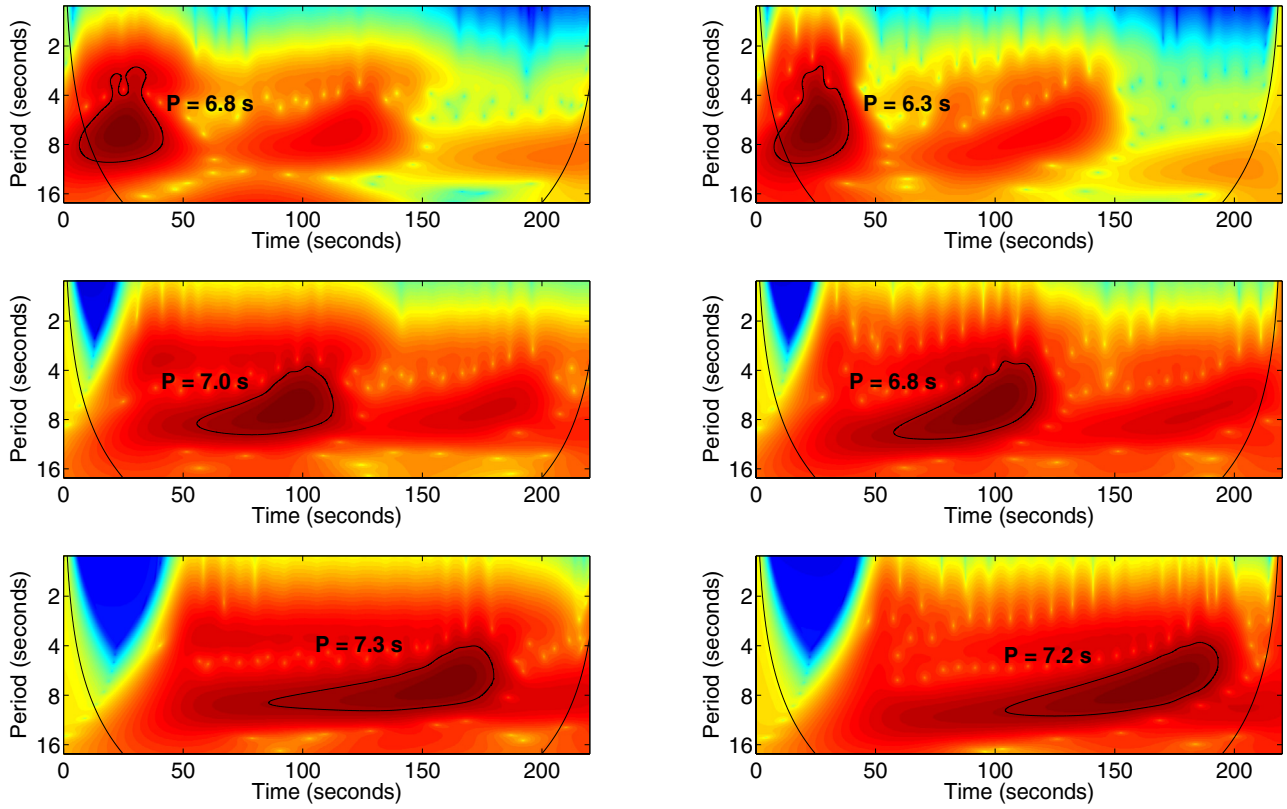

Fig. 11. The "time evolutions" and comparison of tadpole shapes in three different detection points $L_D = L/4, L/2, 3L/4$ (*upper, middle, and lower panel*, respectively). In the *left column*, the results for the density slab are shown, whereas the results for Harris current sheet can be seen in the *right column*.

Acknowledgements. This research has been supported by Grant IAA300030701 of Grant Agency of the Academy of Sciences of the Czech Republic and Grant P209/10/1680 of Grant Agency of the Czech Republic. The wavelet analysis was performed using software written by C. Torrence and G. Compo available at URL http://paos.colorado.edu/research/wavelets.

References

Aschwanden, M. 2004, Phys. Sol. Corona (Chichester, UK: Springer, Praxis Publ.)
Aschwanden, M., Fletcher, L., Schrijver, C. J., & Alexander, D. 1999, ApJ, 520, 880
Chung, T. J. 2002, Comput. Fluid Dyn. (New York, USA: Cambridge University Press)
De Moortel, I., Ireland, J., Walsh, R. W., & Hood, A. W. 2002, Sol. Phys., 209, 61
Edwin, P. M., & Roberts, B. 1982, Sol. Phys., 76, 239
Edwin, P. M., & Roberts, B. 1983, Sol. Phys., 88, 179
Jelínek, P., & Karlický, M. 2009, Eur. Phys. J. D, 54, 305
Jelínek, P., & Karlický, M. 2010, IEEE Trans. Plasma Sci., 38, 2243
Jiřička, K., Karlický, M., Kepka, O., Tlamicha, A. 1993, Sol. Phys., 147, 203
Karlický, M., Jelínek, P., & Mészárosová H. 2011, A&A, 529, A96
Katsiyannis, A. C., Williams, D. R., McAteer, R. T. J., et al. 2003, A&A, 406, 709
Kliem, B., Karlický, M., & Benz, A. O. 2000, A&A, 360, 715
Mészárosová, H., Sawant, H. S., Cecatto, J. R., et al. 2009a, Adv. Space Res., 43, 1479
Mészárosová, H., Karlický, M., Rybák, J., & Jiřička, K. 2009b, ApJ, 697, L108
Mészárosová, H., Karlický, M., Rybák, J., & Jiřička, K. 2009c, A&A, 502, L13
Murawski, K., & Roberts, B. 1994, Sol. Phys., 151, 305
Nakariakov, V. M., & Roberts, B. 1995, Sol. Phys., 159, 399
Nakariakov, V. M., Arber, T. D., Ault, C. E., et al. 2004, MNRAS, 349, 705
Nakariakov, V. M., Pascoe, D. J., & Arber, T. D. 2005, Space Sci. Rev., 121, 115
Ofman, L., & Wang, T. 2002, ApJ, 580, L85
Priest, E. R. 1982, Solar Magnetohydrod (London, England: D. Reidel Publishing Company)
Roberts, B. 1981a, Sol. Phys., 69, 27
Roberts, B. 1981b, Sol. Phys., 69, 39
Roberts, B., Edwin, P. M., & Benz, A. O. 1983, Nature, 305, 688
Roberts, B., Edwin, P. M., & Benz, A. O. 1984, ApJ, 279, 857
Sankaran, K., Martinelli, L., Jardin, S. C., & Choueiri, E. Y. 2002, Int. J. Numer. Meth. Engng., 53, 1415
Sato, T., & Hayashi, T. 1979, Phys. Fluids, 22, 1189
Selwa, M., & Murawski, K. 2004, A&A, 425, 719
Selwa, M., Murawski, K., & Solanki, S. K. 2005, A&A, 436, 701
Selwa, M., Ofman, L., & Murawski, K. 2007, ApJ, 668, L83
Smith, J. M., Roberts, B., & Oliver, R. 1997, A&A, 327, 377
Wang, T. J., & Solanki, S. K. 2004, A&A, 421, L33
Torrence, Ch., & Compo, G. P. 1998, Bull. Am. Meteor. Soc., 79, 61
Zhukov, V. I. 1989, Astrophys. Space Sci., 154, 247